# Organic matter, geochemical, visible spectrocolorimetric properties, radiocesium properties, and grain size of potential source material, target sediment core layers and laboratory mixtures for conducting sediment fingerprinting approaches in the Mano Dam Reservoir (Hayama Lake) catchment, Fukushima Prefecture, Japan.

Thomas Chalaux-Clergue[a], Olivier Evrard[a,*], Roxanne Durand[a], Alison Caumon[a], Seiji Hayashi[b], Hideki Tsuji[b], Sylvain Huon[c], Véronique Vaury[c], Yoshifumi Wakiyama[d], Atsushi Nakao[e], J. Patrick Laceby[f], Irène Lefèvre[a], Yuichi Onda[g]

[a] *Laboratoire des Sciences du Climat et de l'Environnement (LSCE-IPSL), Unité Mixte de Recherche 8212 (CEA-CNRS-UVSQ), Université Paris-Saclay, Gif-sur-Yvette, France*
[b] *National Institute for Environmental Science (NIES), Fukushima Branch, 10-2 Fukasaku, Miharu, Tamura, Fukushima, 963-7700 Japan*
[c] *Sorbonne Universités, Institut d'Ecologie et des Sciences de l'environnement de Paris (iEES), Paris, France*
[d] *Institute of Environmental Radioactivity (IER), University of Fukushima, Fukushima, Japan*
[e] *Graduate School of Life and Environmental Sciences, Kyoto Prefectural University, Kyoto, Japan*
[f] *Environmental Monitoring and Science Division, Alberta Environment and Parks, 3115–12 Street NE, Calgary, Alberta, Canada*
[g] *Center for Research in Isotopes and Environmental Dynamics, University of Tsukuba, Tsukuba, Japan*

## 1. Introduction

The current dataset was compiled to investigate the redistribution of sediments contaminated with radionuclides emitted following the Fukushima Daiichi Nuclear Power Plant (FDNPP) disaster that occurred in March 2011 in northeastern Japan (Onda et al., 2020). The radioactive plume is drained to the Pacific Ocean by several coastal rivers, and sediment-bound radionuclide transfers in these rivers are mainly controlled by the occurrence of typhoons and tropical storms (Evrard et al., 2015; Laceby et al., 2016b). The dataset was mainly generated to understand the temporal changes of land-use and the impact of farmland decontamination on the sources contributions to sediment in the Mano Dam reservoir (37.72167°N, 140.83056°E) catchment (67 $km^2$), before and after the FDNPP accident. To this end, a sediment core was sampled from the lower part of the reservoir on 8 June 2021. As such, this dataset represents an extension of previous work conducted on sediment cores collected in the same reservoir by Huon et al. (2018) in 2014, which was after the FDNPP accident and before decontamination of the catchment.
The current dataset comprises four csv files including data and metadata information and their respective descriptions of variables. The data set is composed of soil samples, sediment core layer and laboratory mixtures. Laboratory mixtures were prepared to provide a dataset to calibrate/validate un-mixing models implemented to address this research question and analysed in the same conditions and using the same equipment as the source/target material (Batista et al., 2022).

The format of this database is part of the discussion of the Thematic School organised in October 2021 (https://www.lsce.ipsl.fr/tracing2021/) and March 2024 (https://www.lsce.ipsl.fr/tracing2024/) to come up with concrete suggestions to improve the design and implementation of sediment fingerprinting or tracing methods. Among these, best practices to share tracing data and samples, which will increase the visibility

*Corresponding author: olivier.evrard@lsce.ipsl.fr (Olivier Evrard)

of the fingerprinting technique in geoscience, are to be promoted (Evrard et al., 2022). The current dataset proposes sediment source fingerprinting database along with the associated metadata for potential source and target material samples registered with an International Geological Sample Number (IGSN) using the SESAR website (https://www.geosamples.org/). The current dataset may provide a template for colleagues from the international scientific community dealing with sediment fingerprinting to share their own data following the proposed unified template format (Evrard et al., 2024, https://doi.org/10.5281/zenodo.10725788).

## 2. Materials and Methods

### 2.1. Catchment description

The Mano Dam reservoir catchment (84 $km^2$), is located in the upper part of the Mano River in northeastern Japan (Fukushima Prefecture, Tōhoku region), is a typical mountainous agricultural catchment of the eastern edge of Fukushima Prefecture (Fig 1 from Chalaux-Clergue et al. (2024)). Due to the steep topography, cropland is located at the bottom of valleys and in the vicinity of rivers, and it is bordered by forest on steep mountainous hillslopes. Forestry is the main land use, which covers 91% of the catchment, while cropland represents 7% and, urban settlements and bare soil less than 2% (JAXA, 2016, 2018, 2022). However, cropland is located in places with a high hydro-sedimentary connectivity (Chartin et al., 2013). The Hayama Lake catchment area is located within the main inland radioactive contamination plume resulting from the Fukushima Daiichi Nuclear Power Plant accident in March 2011 (Kato et al., 2019). Once deposited, $^{137}$Cs strongly and quasi-permanently binds to fine soil particles such as silts and clays (Sawhney, 1972; He & Walling, 1996), which has been confirmed in the soils of Fukushima Prefecture (Saito et al., 2014; Nakao et al., 2014).

Catchment altitude ranges from 170 $m$ to 700 $m$ above sea level. The climate is continental (Dfa), with no dry season and hot summer according to Köppen's climatic classification (Beck et al., 2018). The regional hydrological year runs from November to October (Laceby et al., 2016a; Whitaker et al., 2022). Over the 2006 to 2021 period, the mean annual temperature was 13.6 $\pm$ 0.4 $°C\ y^{-1}$ (standard deviation), with mean monthly values ranging from $-1.5$ $°C$ in January to 31.1 $°C$ in August. The mean annual precipitation was 1220 $\pm$ 189 $mm\ y^{-1}$ (SD), some of which falls as snow in winter. The majority of precipitation occurs between June and October, representing 60% of the annual rainfall and 86% of the rainfall erosivity (Laceby et al., 2016a). This period corresponds to the Japanese typhoon season with a peak of intensity in September in Fukushima Prefecture. Major typhoons were shown to be the main drivers of sediment production (Chartin et al., 2017), as they can generate 40% of the annual rainfall erosivity within a very short period (Laceby et al., 2016a).

The Mano Dam reservoir catchment is mainly underlain by non-alkaline mafic volcanic rocks (42%), granite (31%) granodiorite (17%) and sedimentary rocks (7%). Main soil groups, according to the Comprehensive Soil Classification System of Japan (Obara et al., 2011, 2015, and equivalent soil types according to the World Reference Base for Soil Resources (WRB)), are the following: Brown Forest soils (37%; WRB: Cambisols/Stagnosols), Allophanic Andosols (36%; Silandic Andosols), Cambic Red-Yellow soils (9%; WRB: Cambisols) and Lithosols (9%; WRB: Leptosols) (data from NARO (2011)).

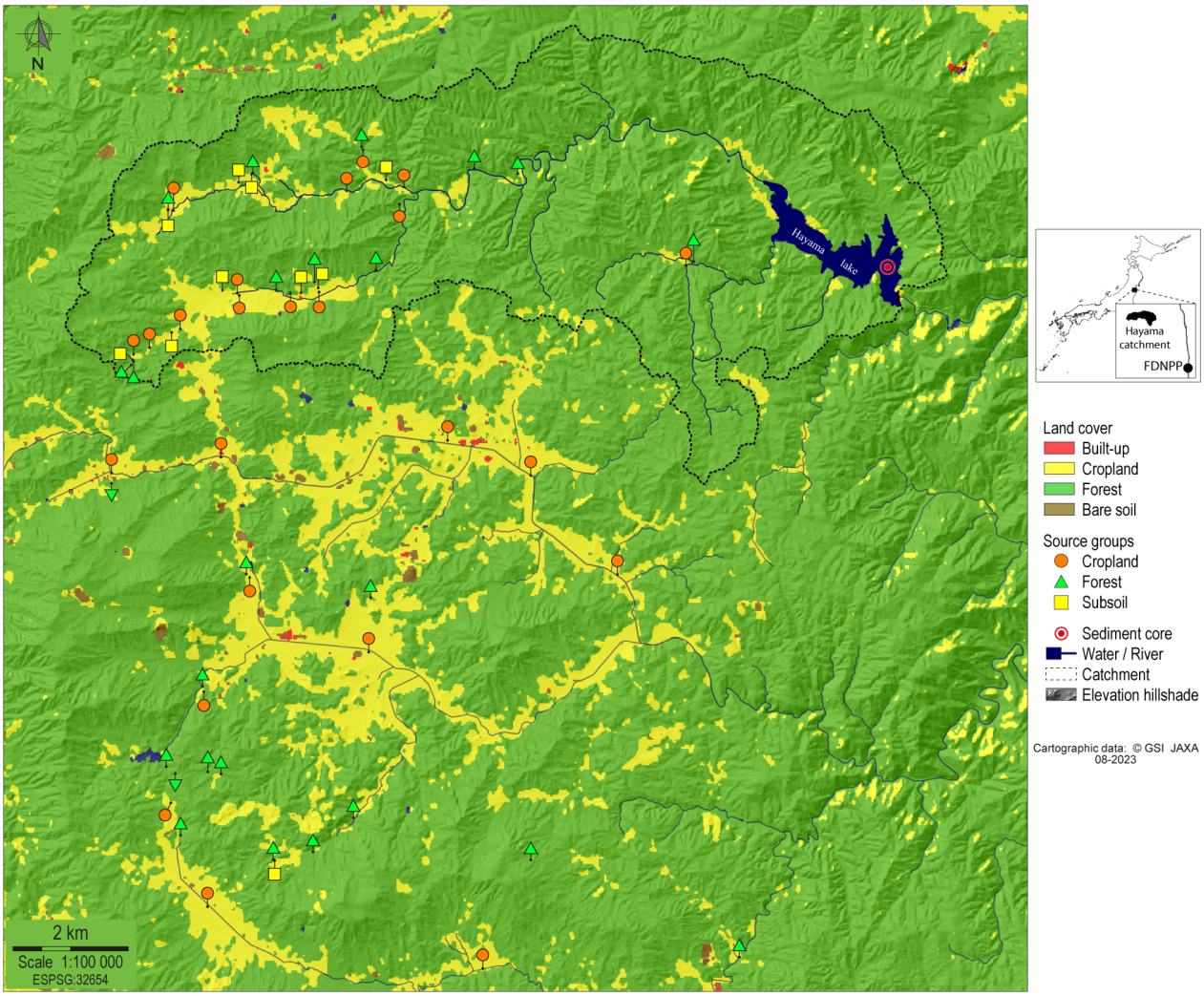


Figure 1: Map of the main land uses in the Mano Dam reservoir catchment area over the 2014-2016 period with location of source samples and the sediment core. Cartographic data: Geospatial Information Authority of Japan (GSI) and JAXA). FDNPP: Fukushima Daiichi nuclear power plant. From Chalaux-Clergue et al. (2024)

### 2.2. Samples

Three potential soil source materials (n = 68) were considered including undecontaminated cropland ($n$ = 24), remediated cropland ($n$ = 10), forest ($n$ = 24) and subsurface material originating from channel bank collapse or landslides ($n$ = 10; referred to as subsoil). The Mano Dam downstream sediment core (IGSN: 10.58052/IETGC00WU) was collected downstream in the Mano Dam lake (Hayama lake) on the 8 June 2021 was 38 $cm$ in length with a diameter of 11 $cm$ and was sectioned into 1-cm layers ($n$ = 38). All soil samples were successively sieved to 2000 $\mu m$ to remove coarse material, and then to 63 $\mu m$. Laboratory mixtures ($n$ = 27) were made to assess different contributions from the three sources among undecontaminated cropland, forest and subsoil.

### 2.3. Radiocesium measurements

Gamma spectrometry with a low-background coaxial HPGe detector was used to determined the $^{134}$Cs and $^{137}$Cs activities in the sediment samples. The counting times ranged from $3 \times 10^4$ to $8 \times 10^4$ $s$. The $^{137}$Cs

and $^{134}$Cs activities were measured at the 605 $keV$ and 662 $keV$ emission peaks, respectively, errors reached about 5 % at 95 % confidence level. All measured counts were corrected for background levels which were, as detector and geometry efficiency, estimated at least every two months. Counting efficiency and quality assurance were implemented using certified International Atomic Energy Agency reference materials prepared in the same containers as the sample. Radiocesium activities were decay-corrected to the sampling date. The $^{134}$Cs and $^{137}$Cs were also decay-corrected to $11^{th}$ March 2011 and $^{134}$Cs/$^{137}$Cs ratio were compared to the ratio 1.06 ± 0.04 (Kobayashi et al., 2013) to further confirm the FDNPP origin.

### 2.4. Organic matter and stable isotopes

In the Mano Dam reservoir catchment, sediment and soils were found not to contain carbonate minerals, and all the carbon associated with particulate matter is organic in nature (Huon et al., 2018). Total organic carbon (TOC) and total nitrogen (TN) elemental concentrations and isotopes ($\delta^{13}$C and $\delta^{15}$N) were determined by a combustion method using a continuous flow elementary analyser (Elementar VarioPyro cube) coupled with an Isotope Ratio Mass Spectrometer (EA-IRMS) (Micromass Isoprime) at the Institute of Ecology and Environmental Sciences (iEES Paris) in France. A first analysis run was conducted to measure TOC concentration together with a set of tyrosine standards (Coplen et al., 1983). The second analysis run was dedicated to measure TN concentration after sample weight optimisation from TOC results. For combustion, oxygen was injected during 70 $s$ (30 mL.min$^{-1}$) at 850 °$C$ for reduction and the combustion furnace at 1120 °$C$ (Agnihotri et al., 2014). The analytical precision was assessed with repeated analyses of a tyrosine intern standard ($n = 51$), calibrated against international reference standards (Girardin & Mariotti, 1991). The uncertainties associated with the calculation of TOC/TN and TN/TOC ratio were calculated with the ratio uncertainty propagation function (eq. 9). The soil source measurements were described in the study of Laceby et al. (2016b). To evaluate the nature of sedimentary organic matter, terrestrial and/or freshwater, the distribution of sample values was plotted in a $\delta^{13}$C (d13C_PrM) vers. TOC/TN diagram and compared to the thresholds reported in Lamb et al. (2006) and (Amorim et al., 2022) thresholds.

### 2.5. Bulk density

Bulk density ($\rho_b$) was determined on fresh sediment using a 1 $cm^3$ ($V$) acrylic cube. Before filling the cube, the *empty weight* ($g$) was reported. Cubes were filled with fresh sediment using a metallic spatula, the *humid weight* ($M_h$ in $g$) was reported, then they were oven-dried at 40 °$C$ for 96 hours (Heraeus T12, Thermo Electron Corporation) and the *dry weight* ($M_d$ in $g$) was measured. The dry bulk density ($\rho_b$ in $g\ cm^{-3}$) in calculated as follows:

$$\rho_b = \frac{M_d}{V} \tag{1}$$

### 2.6. Elemental geochemistry

Elemental geochemistry was determined using X-ray fluorescence (XRF) (Malvern Panalytical, ED-XRF Epsilon 4). A total of 15 elemental concentrations were measured (Al, Ca, Cr, Cu, Fe, K, Mg, Mn, Ni, Rb, Si, Sr, Ti, Zn, and Zr). Measurements were conducted in containers covered with a 3.6 µm thin Mylar film (Chemplex, Mylar Thin-Film cat. no. 157) with a 10 $mm$ exposure surface. A minimum of 0.1 $g$ of material was analysed. To consider the potential heterogeneity within a sample, three replicate measurements were made, and the mean value was calculated. To assess the accuracy of the measurement, a standard (JMS-1, sediment from the Tokyo Bay (Terashima et al., 2002)) was measured every seven samples ($n = 38$) and the accuracy of the measured batch was determined with the calculation of the Root Mean Square Errors (RMSE).

### 2.7. Visible colorimetry

Visible colorimetry was measured using a portable diffuse reflectance spectrophotometer, Kanonica Minolta CM-700d, set on a 3 *mm* target radius. Samples were measured in a plastic zip bag. In order to take into account potential heterogeneity within a sample, three measurements were made at different locations on the bag. The spectrophotometer was calibrated at the start of each set of measurements with a zero (black) and white standards. Measurements were conducted according to the D65 illuminance standard, 10° angle observer and excluding the specular component. The spectral reflectance (in %) was measured from 360 *nm* to 740 *nm* with a 10 *nm* resolution (30 wavelength classes). Raw data was processed using the colour data software CM-S100w SpectraMagic NX (Minolta, 2022). Colour parameters within the Cartesian coordinate systems CIE Lab (1976) (i.e. L*, a* and b*) (CIE, 2008) and CIE LCh (i.e. C* and h) were exported. The CIE LCh is a vector representation of the CIE Lab (1976), where vectors are calculated as follows:

$$\mathrm{C}^* = \sqrt{\mathrm{a}^{*2} + \mathrm{b}^{*2}}, \tag{2}$$

$$\mathrm{h} = \begin{cases} \arctan(b^*/a^*) & \text{if } \arctan(b^*/a^*) \geqslant 0 \\ \arctan(b^*/a^*) + 360 & \text{otherwise} \end{cases} \tag{3}$$

Within the CIE Lab system: L* is the lightness of the colour, from black (0) to white (100), a* is the position between green to red (negative values are associated with green and positives with red), b* is the position between blue and yellow (negative values are associated with blue and positive values with yellow). Within the CIE LCh system: C* is the chroma (positive values are associated to brighter colors and negative values to duller colors) and h is the hue angle (in °) in the CIE Lab color wheel.

The Q7/4 ratio as defined by Debret et al. (2011) was calculated as the ratio between 700 *nm* and 400 *nm* reflectance values, its uncertainty was calculated with equation 5.

The oxy-hydroxide geothite ($\alpha$-FeOOH) peaks at 445 *nm* and 525 *nm* as defined by Debret et al. (2011) were calculated from the first derivative reflectance spectra. For each replicate of the measurement and for each sample, the first derivative reflectance spectra was calculated and smoothed with a Savitzky-Golay filter using the savitzkyGolay function (differentiation order = 1, polynomial order = 3, window size = 5) from R package prospectr (Stevens & Ramirez-Lopez, 2022, ver. 0.2.6) then the mean per sample and the standard deviation were calculated. From the first derivative of reflectance, two geothite peaks were calculated: first, the 445 *nm* peak value was calculated as the mean of values at 440 and 450 *nm*, and the 525 *nm* peak as the mean of those at 520 and 530 *nm*. The uncertainty associated with these peaks was calculated with equation 6.

The remission function was calculated from the reflectance spectra: $f(R) = (1 - R)^2$ according to the Kubelka-Munk relationship (Scheinost et al., 1998). Then, the second derivative was calculated and the spectra was smoothed with a Savitzky-Golay filter using the savitzkyGolay function (differentiation order = 2, polynomial order = 3, window size = 5). From the second derivative of remission function spectra, the iron oxide-associated parameters A1, A2, A3 and the goethite proportion within iron oxides (Gt) were calculated following the approach defined by Tiecher et al. (2015). The peaks A1 and A2 are associated with goethite and A3 with hematite and were calculated as the amplitude between each maximum and minimum bands. Thus A1 is the difference between 450 and 420 *nm*, A2 is the difference of 510 and 480 *nm* and A3 is the difference of 575 (as the mean of 570 and 580 *nm*) and 535 *nm* (as the mean of 530 and 540 *nm*) and Gt as the ratio of A1/(A1+A3). The uncertainty associated with A1 and A2 were calculated with equation 7, A3 uncertainty and Gt uncertainty were calculated with equation 8 and equation 9, respectively.

### 2.8. Particle size

Particle size analyses were performed with a laser diffraction particle size analyser (Mastersizer 3000 with Hydro LV, Malvern Panalytical) in osmotic water on fresh sediment without sonic dispersion. Each sediment sample was measured 5 times. The grain size distribution was measured from 0.01 $\mu m$ to 3500 $\mu m$. It was used to determine the portion of particles which are smaller than 10% (D10), 50% (D50) and 90% (D90) of the whole measured particles. The specific surface area (SSA) was measured under the assumption of spherical shape. It is defined as the total surface area of a solid material divided by its mass. The SSA depends on particle size and also on its structure and porosity.

### 2.9. Uncertainty propagation formulas

Uncertainty ($\Delta$R) was calculated using a propagation of uncertainty equation, with $f$ a set of non-linear combinations of the variables $x$, with the Taylor expansion being:

$$\Delta \mathrm{R} = \sqrt{\sum_{i=1}^{n} \frac{\partial f_i}{\partial x_i} \cdot x_i}, \tag{4}$$

Then, for the calculations conducted in the current research following uncertainty propagation formulas were developed from the Taylor expansion. In theses formulas the following notation referring to A as an analysis (e.g. TOC) and $\Delta$A as its error (e.g. TOC_SD) was used.

Uncertainty Propagation formula for a division:

$$\Delta\Big(\frac{\mathrm{A}}{\mathrm{B}}\Big) = \sqrt{\Big(\frac{1}{B} \cdot \Delta\mathrm{A}\Big)^2 + \Big(-\frac{A}{B^2} \cdot \Delta\mathrm{B}\Big)^2}, \tag{5}$$

Uncertainty Propagation formula for the mean of two values:

$$\Delta\Big(\frac{\mathrm{A}+\mathrm{B}}{2}\Big) = \sqrt{\Big(\frac{1}{2} \cdot \Delta\mathrm{A}\Big)^2 + \Big(-\frac{1}{2} \cdot \Delta\mathrm{B}\Big)^2}, \tag{6}$$

Uncertainty Propagation formula for a difference:

$$\Delta(\mathrm{A}-\mathrm{B}) = \sqrt{(\Delta\mathrm{A})^2 + (-\Delta\mathrm{B})^2}, \tag{7}$$

Uncertainty Propagation formula for a difference of means:

$$\Delta\Big(\frac{\mathrm{A}+\mathrm{B}}{2} - \frac{\mathrm{C}+\mathrm{D}}{2}\Big) = \sqrt{\Big(\frac{1}{2} \cdot \Delta\mathrm{A}\Big)^2 + \Big(\frac{1}{2} \cdot \Delta\mathrm{B}\Big)^2 + \Big(-\frac{1}{2} \cdot \Delta\mathrm{C}\Big)^2 + \Big(-\frac{1}{2} \cdot \Delta\mathrm{D}\Big)^2}, \tag{8}$$

Propagation of uncertainty for a proportion:

$$\Delta\Big(\frac{\mathrm{A}}{\mathrm{A}+\mathrm{B}}\Big) = \sqrt{\Big(\frac{B}{(A+B)^2} \cdot \Delta\mathrm{A}\Big)^2 + \Big(-\frac{A}{(A+B)^2} \cdot \Delta\mathrm{B}\Big)^2}, \tag{9}$$

All processing was achieved using R programming environment (R Core Team, 2022, ver. 4.2.2) within RStudio (RStudio Team, 2023, ver. 2023.06.1.524).

### 2.10. Mapping

Lithological and pedological classifications of soil samples were obtained through location-based extraction from the Fukushima 1:200.000 geological map (Kubo et al., 2003) and the 1:50.000 pedological map (NARO, 2011), respectively. Soil pedologic classes correspond to the English translations of Japanese soil type names according to the Comprehensive Soil Classification System of Japan (Obara et al., 2011). All map processing was conducted in QGIS (QGIS Development Team, 2022, ver 3.26.0).

## 3. Acknowledgements

The assistance provided by Dr. H. Funaki and Dr. K. Yoshimura from the Japan Atomic Energy Agency) in conducting the sediment core sampling in the Mano Dam reservoir is gratefully acknowledged.

## 4. Financial support

The collection and the analysis of the soil and sediment samples were funded by the TOFU (ANR-11-JAPN-001) and the AMORAD (ANR-11-RSNR-0002) projects, under the supervision of the French National Research Agency (ANR, Agence Nationale de la Recherche). The support of CEA (Commissariat à l'Energie Atomique et aux Energies Alternatives, France), CNRS (Centre National de la Recherche Scientifique, France) and JSPS (Japan Society for the Promotion of Science) through the funding of PhD fellowships (H. Lepage, H. Jaegler, T. Chalaux Clergue) and collaboration projects (grant no. PRC CNRS JSPS 2019-2020, no.10; CNRS International Research Project – IRP – MITATE Lab) is also gratefully acknowledged. This work was also supported by ERAN (Environmental Radioactivity Research Network Center) grants I-21-22 and I-22-24, and a mini-project from the FIRE (Fédération Ile-de-France de Recherche en Environnement - CNRS FR3020 FIRE, France) entitled RICOR ('Reconstructing the Impact of Changing land Occupation on the fate of Radionuclides').

## References

Agnihotri, R., Kumar, R., Prasad, M. V. S. N., Sharma, C., Bhatia, S. K., & Arya, B. C. (2014). Experimental Setup and Standardization of a Continuous Flow Stable Isotope Mass Spectrometer for Measuring Stable Isotopes of Carbon, Nitrogen and Sulfur in Environmental Samples. *MAPAN*, *29*, 195–205. URL: http://link.springer.com/10.1007/s12647-014-0099-8. doi:10.1007/s12647-014-0099-8.

Amorim, H. C., Hurtarte, L. C., Souza, I. F., & Zinn, Y. L. (2022). C:N ratios of bulk soils and particle-size fractions: Global trends and major drivers. *Geoderma*, *425*, 116026. URL: https://linkinghub.elsevier.com/retrieve/pii/S0016706122003330. doi:10.1016/j.geoderma.2022.116026.

Batista, P. V. G., Laceby, J. P., & Evrard, O. (2022). How to evaluate sediment fingerprinting source apportionments. *Journal of Soils and Sediments*, *22*, 1315–1328. URL: https://link.springer.com/10.1007/s11368-022-03157-4. doi:10.1007/s11368-022-03157-4.

Beck, H. E., Zimmermann, N. E., McVicar, T. R., Vergopolan, N., Berg, A., & Wood, E. F. (2018). Present and future Köppen-Geiger climate classification maps at 1-km resolution. *Scientific Data*, *5*, 180214. URL: http://www.nature.com/articles/sdata2018214. doi:10.1038/sdata.2018.214.

Chalaux-Clergue, T., Bizeul, R., Batista, P. V. G., Martínez-Carreras, N., Laceby, J. P., & Evrard, O. (2024). Sensitivity of source sediment fingerprinting to tracer selection methods. *SOIL*, *10*, 109–138. URL: https://soil.copernicus.org/articles/10/109/2024/. doi:10.5194/soil-10-109-2024.

Chartin, C., Evrard, O., Laceby, J. P., Onda, Y., Ottlé, C., Lefèvre, I., & Cerdan, O. (2017). The impact of typhoons on sediment connectivity: Lessons learnt from contaminated coastal catchments of the Fukushima Prefecture (Japan): Typhoon Impact on Sediment Connectivity - Fukushima, Japan. *Earth Surface Processes and Landforms*, *42*, 306–317. URL: https://onlinelibrary.wiley.com/doi/10.1002/esp.4056. doi:10.1002/esp.4056.

Chartin, C., Evrard, O., Onda, Y., Patin, J., Lefèvre, I., Ottlé, C., Ayrault, S., Lepage, H., & Bonté, P. (2013). Tracking the early dispersion of contaminated sediment along rivers draining the Fukushima radioactive pollution plume. *Anthropocene*, *1*, 23–34. URL: https://linkinghub.elsevier.com/retrieve/pii/S2213305413000088. doi:10.1016/j.ancene.2013.07.001.

CIE (2008). C. I. C.: Colorimetry — Part 4: CIE 1976 L*a*b* Colour space. doi:ISO/CIE11664-4:2019(E).

Coplen, T. B., Kendall, C., & Hopple, J. (1983). Comparison of stable isotope reference samples. *Nature*, *302*, 236–238. URL: https://www.nature.com/articles/302236a0. doi:10.1038/302236a0.

Debret, M., Sebag, D., Desmet, M., Balsam, W., Copard, Y., Mourier, B., Susperrigui, A.-S., Arnaud, F., Bentaleb, I., Chapron, E., Lallier-Vergès, E., & Winiarski, T. (2011). Spectrocolorimetric interpretation of sedimentary dynamics: The new "Q7/4 diagram". *Earth-Science Reviews*, *109*, 1–19. URL: https://linkinghub.elsevier.com/retrieve/pii/S0012825211000985. doi:10.1016/j.earscirev.2011.07.002.

Evrard, O., Batista, P. V. G., Company, J., Dabrin, A., Foucher, A., Frankl, A., García-Comendador, J., Huguet, A., Lake, N., Lizaga, I., Martínez-Carreras, N., Navratil, O., Pignol, C., & Sellier, V. (2022). Improving the design and implementation of sediment fingerprinting studies: Summary and outcomes of the TRACING 2021 Scientific School. *Journal of Soils and Sediments*, *22*, 1648–1661. URL: https://link.springer.com/10.1007/s11368-022-03203-1. doi:10.1007/s11368-022-03203-1.

Evrard, O., Chalaux-Clergue, T., Bizeul, R., & Foucher, A. (2024). An unified template for sediment source fingerprinting databases. URL: https://zenodo.org/doi/10.5281/zenodo.10725788. doi:10.5281/ZENODO.10725788.

Evrard, O., Laceby, J. P., Lepage, H., Onda, Y., Cerdan, O., & Ayrault, S. (2015). Radiocesium transfer from hillslopes to the Pacific Ocean after the Fukushima Nuclear Power Plant accident: A review. *Journal of Environmental Radioactivity*, *148*, 92–110. URL: https://linkinghub.elsevier.com/retrieve/pii/S0265931X1530031X. doi:10.1016/j.jenvrad.2015.06.018.

Girardin, C., & Mariotti, A. (1991). Analyse isotopique du 13C en abondance naturelle dans le carbone organique: un système automatique avec robot préparateur}. *Cahiers ORSTOM, Serie Pedologie*, *26*, 371–380. URL: https://www.documentation.ird.fr/hor/fdi:39457.

He, Q., & Walling, D. (1996). Interpreting particle size effects in the adsorption of 137Cs and unsupported 210Pb by mineral soils and sediments. *Journal of Environmental Radioactivity*, *30*, 117–137. URL: https://linkinghub.elsevier.com/retrieve/pii/0265931X96892757. doi:10.1016/0265-931X(96)89275-7.

Huon, S., Hayashi, S., Laceby, J. P., Tsuji, H., Onda, Y., & Evrard, O. (2018). Source dynamics of radiocesium-contaminated particulate matter deposited in an agricultural water reservoir after the Fukushima nuclear accident. *Science of The Total Environment*, *612*, 1079–1090. URL: https://linkinghub.elsevier.com/retrieve/pii/S0048969717319083. doi:10.1016/j.scitotenv.2017.07.205.

JAXA (2016). High-Resolution Land-Use and Land-Cover Map of Japan [2006 ~ 2011] (ver. 16.09; 10-m resolution; 12 categories). URL: https://www.eorc.jaxa.jp/ALOS/en/dataset/lulc/lulc_jpn_e.htm.

JAXA (2018). High-Resolution Land-Use and Land-Cover Map of Japan [2014 ~ 2016] (ver. 18.03; 30-m resolution; 12 categories). URL: https://www.eorc.jaxa.jp/ALOS/en/dataset/lulc/lulc_v1803_e.htm.

JAXA (2022). High-Resolution Land-Use and Land-Cover Map of Japan [2018 ∼ 2020] (ver. 21.11; 10-m resolution; 12 categories). URL: https://www.eorc.jaxa.jp/ALOS/en/dataset/lulc/lulc_v2111_e.htm.

Kato, H., Onda, Y., Gao, X., Sanada, Y., & Saito, K. (2019). Reconstruction of a Fukushima accident-derived radiocesium fallout map for environmental transfer studies. *Journal of Environmental Radioactivity*, *210*, 105996. URL: https://linkinghub.elsevier.com/retrieve/pii/S0265931X18303308. doi:10.1016/j.jenvrad.2019.105996.

Kobayashi, T., Nagai, H., Chino, M., & Kawamura, H. (2013). Source term estimation of atmospheric release due to the Fukushima Dai-ichi Nuclear Power Plant accident by atmospheric and oceanic dispersion simulations: Fukushima NPP Accident Related. *Journal of Nuclear Science and Technology*, *50*, 255–264. URL: http://www.tandfonline.com/doi/abs/10.1080/00223131.2013.772449. doi:10.1080/00223131.2013.772449.

Kubo, K., Yanagisawa, Y., Yamamoto, T., Komazawa, M., Hiroshima, T., & Sudo, S. (2003). Fukushima 1:200.000 geological map. URL: https://www.gsj.jp/Map/EN/geology2-2.html#Fukushima.

Laceby, J. P., Chartin, C., Evrard, O., Onda, Y., Garcia-Sanchez, L., & Cerdan, O. (2016a). Rainfall erosivity in catchments contaminated with fallout from the Fukushima Daiichi nuclear power plant accident. *Hydrology and Earth System Sciences*, *20*, 2467–2482. URL: https://hess.copernicus.org/articles/20/2467/2016/. doi:10.5194/hess-20-2467-2016.

Laceby, J. P., Huon, S., Onda, Y., Vaury, V., & Evrard, O. (2016b). Do forests represent a long-term source of contaminated particulate matter in the Fukushima Prefecture? *Journal of Environmental Management*, *183*, 742–753. URL: https://linkinghub.elsevier.com/retrieve/pii/S0301479716306661. doi:10.1016/j.jenvman.2016.09.020.

Lamb, A. L., Wilson, G. P., & Leng, M. J. (2006). A review of coastal palaeoclimate and relative sea-level reconstructions using $\delta$13C and C/N ratios in organic material. *Earth-Science Reviews*, *75*, 29–57. URL: https://linkinghub.elsevier.com/retrieve/pii/S0012825205001376. doi:10.1016/j.earscirev.2005.10.003.

Minolta, K. (2022). QCM-S100w SpectraMagic NX. Konica Minolta. URL: https://www.konicaminolta.com/instruments/download/software/color/810smnx/.

Nakao, A., Ogasawara, S., Sano, O., Ito, T., & Yanai, J. (2014). Radiocesium sorption in relation to clay mineralogy of paddy soils in Fukushima, Japan. *Science of The Total Environment*, *468–469*, 523–529. URL: https://linkinghub.elsevier.com/retrieve/pii/S0048969713009893. doi:10.1016/j.scitotenv.2013.08.062.

NARO (2011). Comprehensive soil map of agricultural land at 1:50,000 scale (Prefecture and National). URL: https://soil-inventory.rad.naro.go.jp/download5.html.

Obara, H., Maejima, Y., Kohyama, K., Ohkura, T., & Takata, Y. (2015). Outline of the Comprehensive Soil Classification System of Japan – First Approximation. *Japan Agricultural Research Quarterly: JARQ*, *49*, 217–226. URL: https://www.jstage.jst.go.jp/article/jarq/49/3/49_217/_article. doi:10.6090/jarq.49.217.

Obara, H., Ohkura, T., Takata, Y., Kohyama, K., Maejima, Y., & Hamazaki, T. (2011). Comprehensive soil classification system of Japan first approximation. *Nogyo Kankyo Gijutsu Kenkyusho Hokoku = Bulletin of National Institute for Agro-Environmental Sciences*, (pp. 1–73). URL: http://www.niaes.affrc.go.jp/sinfo/publish/public_e.html.

Onda, Y., Taniguchi, K., Yoshimura, K., Kato, H., Takahashi, J., Wakiyama, Y., Coppin, F., & Smith, H. (2020). Radionuclides from the Fukushima Daiichi Nuclear Power Plant in terrestrial systems. *Nature Reviews Earth & Environment*, *1*, 644–660. URL: https://www.nature.com/articles/s43017-020-0099-x. doi:10.1038/s43017-020-0099-x.

QGIS Development Team (2022). QGIS Geographic Information System. Open Source Geospatial Foundation. URL: https://www.qgis.org/fr/site/.

R Core Team (2022). A Language and Environment for Statistical Computing. R Foundation for Statistical Computing. URL: https://www.R-project.org/.

RStudio Team (2023). RStudio: Integrated Development Environment for R. RStudio. URL: http://www.rstudio.com/.

Saito, T., Makino, H., & Tanaka, S. (2014). Geochemical and grain-size distribution of radioactive and stable cesium in Fukushima soils: Implications for their long-term behavior. *Journal of Environmental Radioactivity*, *138*, 11–18. URL: https://linkinghub.elsevier.com/retrieve/pii/S0265931X14002306. doi:10.1016/j.jenvrad.2014.07.025.

Sawhney, B. L. (1972). Selective Sorption and Fixation of Cations by Clay Minerals: A Review. *Clays and Clay Minerals*, *20*, 93–100. URL: https://doi.org/10.1346/CCMN.1972.0200208. doi:10.1346/CCMN.1972.0200208.

Scheinost, A. C., Chavernas, A., Barrón, V., & Torrent, J. (1998). Use and Limitations of Second-Derivative Diffuse Reflectance Spectroscopy in the Visible to Near-Infrared Range to Identify and Quantify Fe Oxide Minerals in Soils. *Clays and Clay Minerals*, *46*, 528–536. URL: http://link.springer.com/10.1346/CCMN.1998.0460506. doi:10.1346/CCMN.1998.0460506.

Stevens, A., & Ramirez-Lopez, L. (2022). An introduction to the prospectr package. URL: https://cran.r-project.org/web/packages/prospectr/vignettes/prospectr.html.

Terashima, S., Imai, N., Taniguchi, M., Okai, T., & Nishimura, A. (2002). The Preparation and Preliminary Characterisation of Four New Geological Survey of Japan Geochemical Reference Materials: Soils, JSO-1 and JSO-2; and Marine Sediments, JMS-1 and JMS-2. *Geostandards Newsletter*, *26*, 85–94. URL: https://onlinelibrary.wiley.com/doi/10.1111/j.1751-908X.2002.tb00626.x. doi:10.1111/j.1751-908X.2002.tb00626.x.

Tiecher, T., Caner, L., Minella, J. P. G., & dos Santos, D. R. (2015). Combining visible-based-color parameters and geochemical tracers to improve sediment source discrimination and apportionment. *Science of The Total Environment*, *527–528*, 135–149. URL: https://linkinghub.elsevier.com/retrieve/pii/S0048969715300401. doi:10.1016/j.scitotenv.2015.04.103.

Whitaker, A. C., Chapasa, S. N., Sagras, C., Theogene, U., Veremu, R., & Sugiyama, H. (2022). Estimation of baseflow recession constant and regression of low flow indices in eastern Japan. *Hydrological Sciences Journal*, *67*, 191–204. URL: https://www.tandfonline.com/doi/full/10.1080/02626667.2021.2003368. doi:10.1080/02626667.2021.2003368.